Electronic Supplementary Material (ESI) for Chemical Science.
This journal is © The Royal Society of Chemistry 2017

Radical-promoted formation of a molecular lasso

Yuping Wang,[†] Junling Sun,[†] Zhichang Liu,[†] Majed S. Nassar,[§]
Youssry Y. Botros,[§,⊥] and J. Fraser Stoddart*[,†]

[†]*Department of Chemistry, Northwestern University, 2145 Sheridan Road, Evanston, Illinois 60208, USA*
[§]*Joint Center of Excellence in Integrated Nano-Systems (JCIN), King Abdul-Aziz City for Science and Technology (KACST), P.O. Box 6086, Riyadh 11442, KSA*
[⊥]*University Research Office, Intel Corporation, Building RNB-6-61, 2200 Mission College Boulevard, Santa Clara, California 95054, USA*

*E-mail: stoddart@northwestern.edu

Supporting Information

Table of Contents

1. Materials and General Methods

Chemicals were purchased as reagent grade and used without further purification. Commercial grades of anhydrous MeCN and *N*,*N*-dimethylformamide (DMF) were used as solvents in all reactions. Compounds **4**•4PF_6,[1] **5**•2PF_6,[2] **6**•2PF_6[3] and **7**[4] were prepared according to literature procedures. Thin layer chromatography (TLC) was performed on silica gel 60F254 (E Merck). Column chromatography was carried out on silica gel 60F (Merck 9385, 0.040–0.063 mm). High performance liquid chromatography (HPLC) was performed on a preparative RP-HPLC instrument, using a C_{18} column (Agilent, 10μm packing, 30 mm × 250 mm). The eluents employed were MeCN and H_2O, both mixed with 0.1 % (v/v) trifluoroacetic acid (TFA). The detector was set to λ = 254 nm. HPLC Analysis was performed on an analytical RP-HPLC instrument, using a C_{18} column. For UV/Vis/Near Infrared (NIR) studies, all sample preparations were performed in an Argon-filled atmosphere. Samples were loaded into quartz 1 cm tubes and sealed with a clear ridged UV doming epoxy (IllumaBond 60-7160RCL) and used immediately after preparation. Nuclear magnetic resonance (NMR) spectra were recorded at 298 K on Bruker Avance 500 spectrometers, with working frequencies of 500 MHz for ^{1}H, and 125 MHz for ^{13}C nuclei, respectively. Chemical shifts are reported in ppm relative to the signals corresponding to the residual non-deuterated solvents.[2] High-resolution mass spectra were measured on an Agilent 6210 Time-of-Flight (TOF) LC-MS, using an ESI source, coupled with Agilent 1100 HPLC stack, using direct infusion (0.6 mL min^{-1} Measurements at X-band (9.5 GHz) were performed with a Bruker Elexsys E580, equipped with a variable Q dielectric resonator (ER-4118X-MD5-W1). Cyclic voltammetry experiments were performed on a Princeton Applied Research 263 A Multipurpose instrument interfaced to a PC, using a glassy carbon working electrode (0.071 cm^2, Cypress system). The electrode surface was polished routinely with an alumina/water slurry on a felt

surface immediately before use. The counter electrode was a Pt coil and the reference electrode was an AgCl coated Ag wire. The concentrations of the samples were 1 mM in 100 mM electrolyte solutions of tetrabutylammonium hexafluorophosphate ($TBAPF_6$) in MeCN.

2. Synthetic Protocols

Scheme S1. One-step synthesis of 3•4PF$_6$ from 6•2PF$_6$ and 7

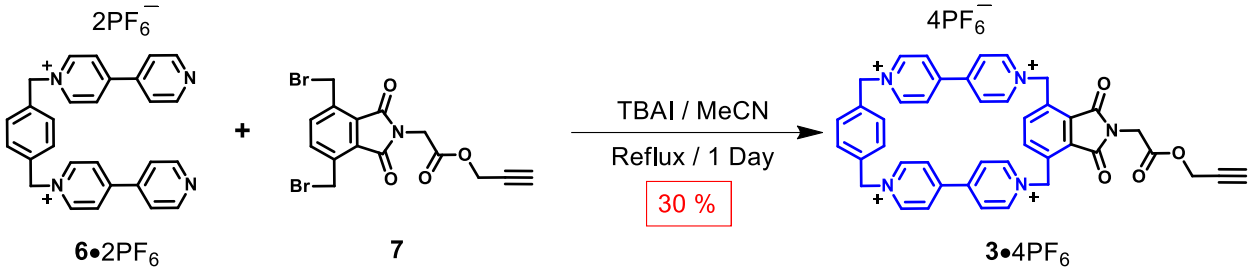

3•4PF$_6$: Compound **6**•2PF$_6$ (70 mg, 0.1 mmol) and **7** (43 mg, 0.1 mmol) were dissolved in MeCN (5 mL), and tetrabutylammonium iodide (3.7 mg, 0.01 mmol) was added to the solution as the catalyst. The reaction mixture was stirred for 1 day under reflux. The solvent was removed by evaporation, and the residue purified by column chromatography (SiO_2: 2 % w/v MeCN solution of NH_4PF_6 as the eluent). The major component was collected, the solvent removed under vacuum, and the solid re-dissolved in H_2O prior to precipitation with an excess of NH_4PF_6. The precipitate was collected by filtration and washed with H_2O, MeOH and finally Et_2O to afford **3**•4PF$_6$ as an off-white solid (34 mg, 30 %). ^{1}H NMR (500 MHz, CD_3CN): δ = 8.90 (d, *J* = 7.5 Hz, 8H), 8.20 (d, *J* = 5.0 Hz, 4H), 8.14 (d, *J* = 5.0 Hz, 4H), 8.13 (s, 2H), 7.51 (s, 4H), 6.22 (s, 4H), 5.77 (s, 4H), 4.74 (d, *J* = 5.0 Hz, 2H), 4.35 (s, 2H), 2.67 (t, *J* = 5.0 Hz, 1H). ^{13}C NMR (126 MHz, CD_3CN): δ = 167.2, 167.0, 150.4, 150.4, 146.7, 145.7, 138.4, 136.5, 134.0, 131.1, 130.7, 128.1, 127.5, 77.6, 76.5, 65.2, 59.9, 53.7, 39.4. HRMS (ESI): *m/z* calcd for $C_{43}H_{35}F_{18}N_5O_4P_3$ $[M - PF_6]^+$ 1120.1614, found 1120.1628.

Scheme S2. One-step synthesis of 1•6PF$_6$ from 5•2PF$_6$ and 3•4PF$_6$

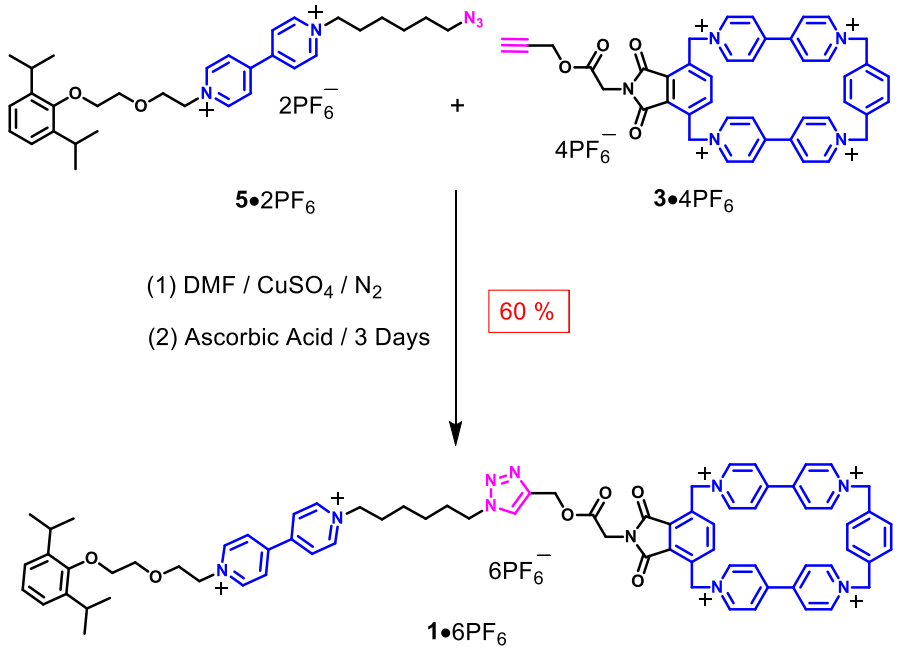

1•2PF$_6$: A solution of $CuSO_4$ (2 mg, 0.012 mmol) in DMF (10 mL) was added to **5**•2PF$_6$ (24 mg, 0.03 mmol) and **3**•4PF$_6$ (39 mg, 0.03 mmol) dissolved in DMF (5 mL). After stirring for 30 min under a N_2 atmosphere, excess of ascorbic acid was added. The reaction mixture was stirred for 3 days at room temperature. Me_2CO was added and the resulting precipitate filtered, re-dissolved in H_2O, and re-precipitated by the addition of an excess of NH_4PF_6. The precipitate was collected by filtration and washed with H_2O, MeOH and finally Et_2O to afford **1**•6PF$_6$ as a white solid (38 mg, 60 %). ^{1}H NMR (500 MHz, CD_3CN): δ = 8.98 (d, *J* = 5.0 Hz, 2H), 8.89 (m, 10H), 8.41 (d, *J* = 5.0 Hz, 2H), 8.39 (d, *J* = 5.0 Hz, 2H), 8.20 (d, *J* = 5.0 Hz, 4H), 8.15 (d, *J* = 5.0 Hz, 4H), 8.05 (s, 2H), 7.88 (s, 1H), 7.50 (s, 4H), 7.12–7.17 (m, 3H), 6.21 (s, 4H), 5.77 (s, 4H), 5.29 (s, 2H), 4.88 (t, *J* = 5.0 Hz, 2H), 4.62 (t, *J* = 5.0 Hz, 2H), 4.41 (t, *J* = 5.0 Hz, 2H), 4.34 (s, 2H), 4.12 (t, *J* = 5.0 Hz, 2H), 3.85–3.89 (m, 4H), 3.32 (qui, *J* = 5.0 Hz, 2H), 2.06 (m, 2H), 1.96 (m, 2H), 1.40 – 1.50 (m, 4H), 1.20 (d, 12H). ^{13}C NMR (126 MHz, CD_3CN): δ = 167.3, 153.4, 151.8, 150.4, 146.9, 146.8, 146.5, 146.3, 145.7, 142.3, 138.2, 136.5, 134.9, 133.9, 131.0, 130.7, 128.2, 128.1, 127.9, 127.8, 127.6, 127.3 125.5, 124.7, 122.4, 74.1, 71.0, 69.3, 65.1, 64.6, 62.4, 59.8, 59.3, 50.3, 39.5, 30.5, 30.2, 26.6, 26.0, 23.9. HRMS (ESI): *m/z* calcd for $C_{75}H_{80}F_{24}N_{10}O_6P_6$ $[M - 2PF_6]^{2+}$ 898.2409, found 898.2416.

Scheme S3. One-step synthesis of 2•6PF$_6$ from 5•2PF$_6$ and 4•4PF$_6$

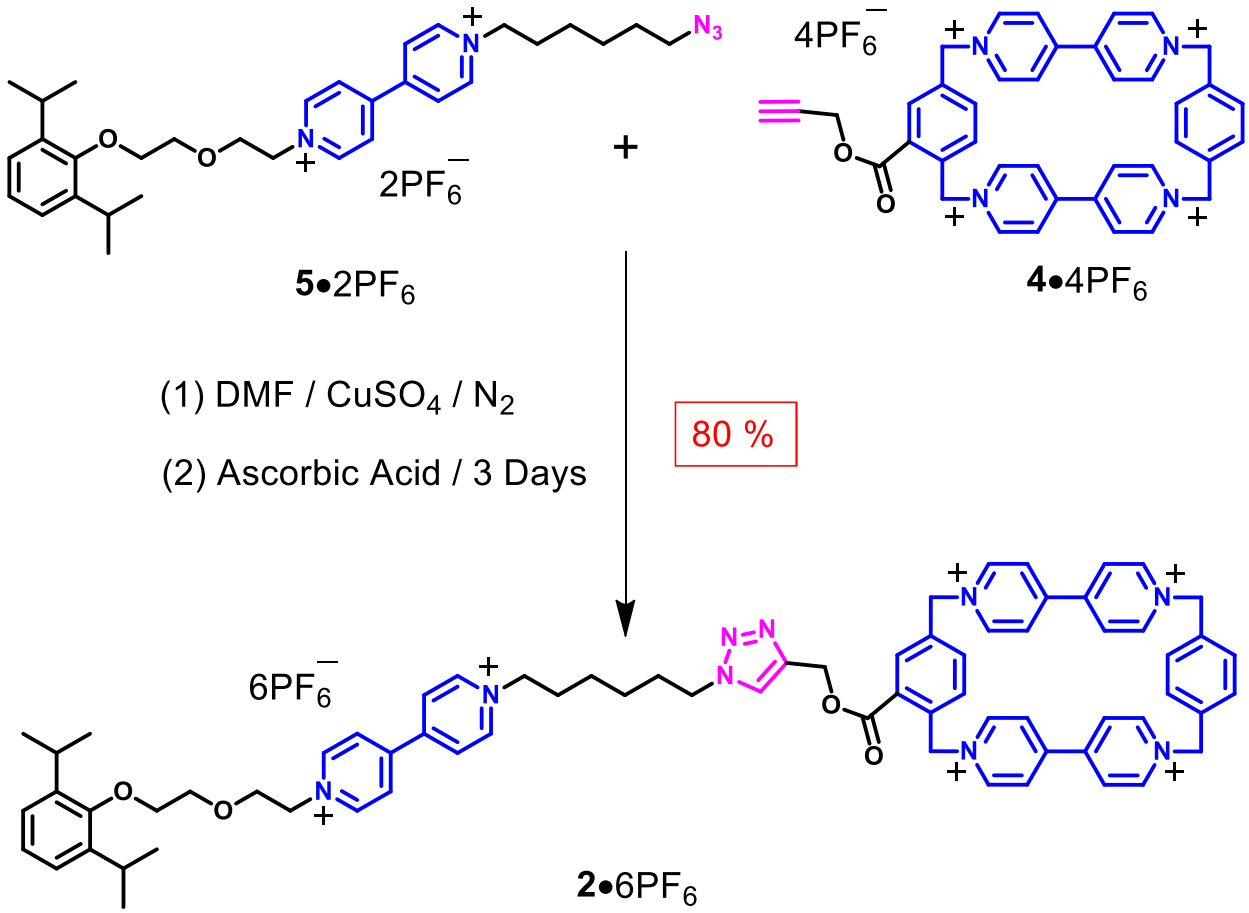

2•6PF$_6$: A solution of $CuSO_4$ (2 mg, 0.012 mmol) in DMF (10 mL) was added to **5**•2PF$_6$ (24 mg, 0.03 mmol) and **4**•4PF$_6$ (35 mg, 0.03 mmol) dissolved in DMF (6 mL). After stirring for 30 min under a N_2 atmosphere, excess of ascorbic acid was added. The reaction mixture was stirred for 3 days at room temperature. Me_2CO was added and the resulting precipitate filtered, re-dissolved in H_2O, and re-precipitated by the addition of an excess of NH_4PF_6. The precipitate was collected by filtration and washed with H_2O, MeOH and finally Et_2O to afford **2**•6PF$_6$ as a white solid (48 mg, 80 %). ^{1}H NMR (500 MHz, CD_3COCD_3): δ = 9.43 (d, *J* = 5.0 Hz, 2H), 9.41 (d, *J* = 5.0 Hz, 2H), 9.37 (d, *J* = 5.0 Hz, 2H), 9.34 (d, *J* = 5.0 Hz, 2H). 9.33 (d, *J* = 5.0 Hz, 2H), 9.27 (d, *J* = 5.0 Hz, 2H), 8.84 (d, *J* = 5.0 Hz, 2H), 8.80 (d, *J* = 5.0 Hz, 2H), 8.53–8.56 (m, 6H), 8.46 (d, *J* = 5.0 Hz, 2H), 8.12 (s, 1H), 7.65–7.81 (m, 7H), 7.06–7.13 (m, 3H), 6.48 (s, 2H), 6.23 (s, 2H), 6.13 (s, 4H), 5.47 (s, 2H), 5.22 (t, *J* = 7.5 Hz, 2H), 4.95 (t, *J* = 7.5 Hz, 2H), 4.46 (t, *J* = 7.5 Hz, 2H), 4.32 (t, *J* =

7.5 Hz, 2H), 3.92–3.95 (m, 4H), 3.35 (m, 2H) 2.20–2.24 (br, 2H), 1.97 (t, J = 7.5 Hz, 2H), 1.56–1.61 (m, 2H), 1.46–1.50 (m, 2H), 1.17 (d, J = 5.0 Hz, 12H). ^{13}C NMR (126 MHz, CD_3CN): δ = 166.3, 153.4, 150.8, 150.1, 146.7, 146.5, 146.1, 146.0, 145.9, 145.8, 142.3, 136.5, 133.0, 131.0, 130.9, 130.8, 128.1, 128.0, 127.9, 127.8, 127.5, 127.3, 125.5, 124.7, 74.1, 71.0, 69.3, 65.2, 64.6, 62.5, 62.4, 59.7, 58.9, 58.9, 58.9, 50.4, 31.3, 30.2, 26.6, 26.0, 25.5, 23.9, 23.9, 19.9, 13.4. HRMS (ESI): *m/z* calcd for $C_{72}H_{79}F_{24}N_9O_4P_4$ $[M - 2PF_6]^{2+}$ 856.7405, found 856.7414.

3. HPLC and HR-MS Spectra of 1•6PF$_6$ and 2•6PF$_6$

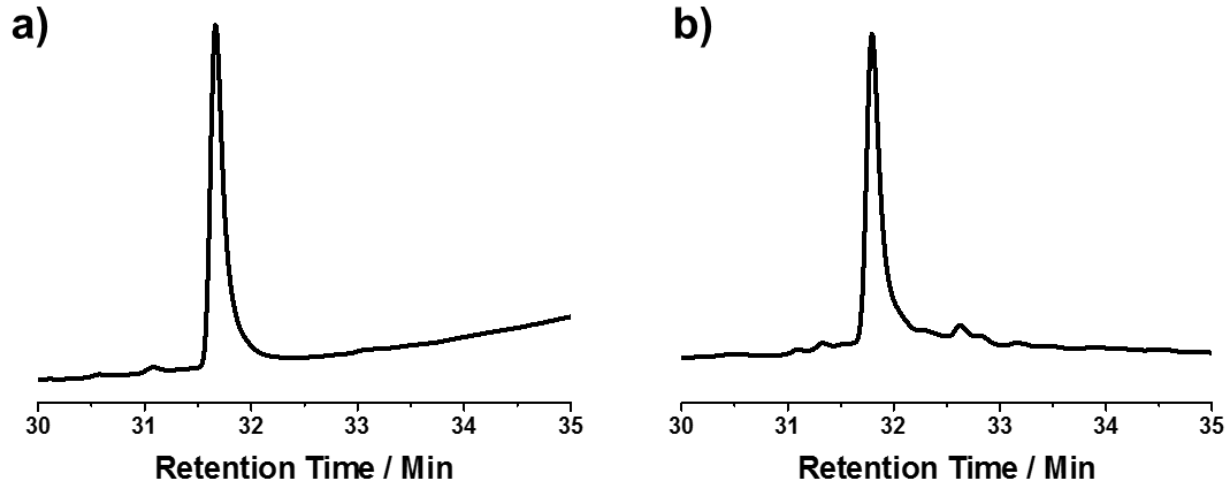

Figure S1. Analytical RP-HPLC chromatograms (H_2O–MeCN, 0.1% TFA, 0–100% MeCN in 60 min, λ = 254 nm) of a) **1**•6PF$_6$, b) **2**•6PF$_6$.

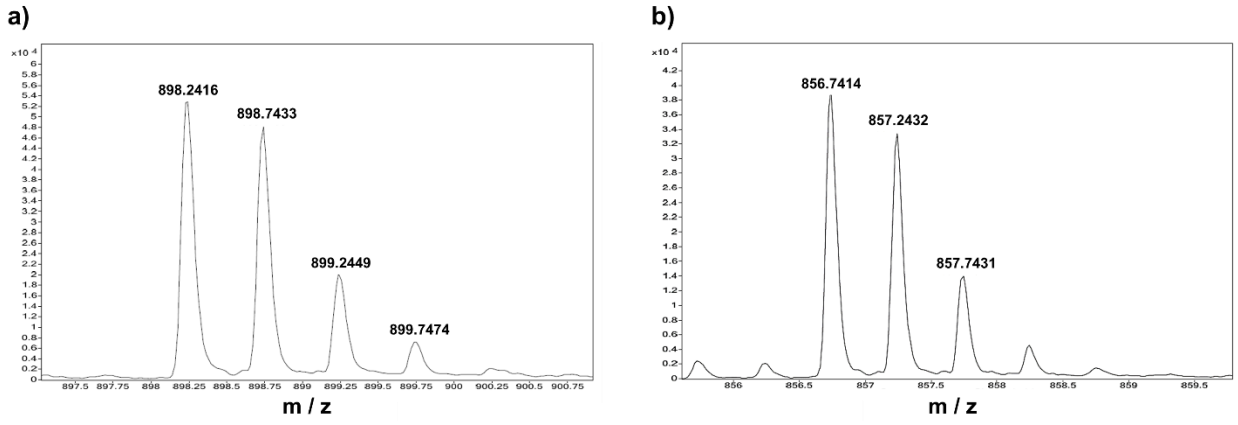

Figure S2. HRMS (ESI) of a) **1**•6PF$_6$. Calculated for $C_{75}H_{80}F_{24}N_{10}O_6P_6$: 898.2409 $[M - 2PF_6]^{2+}$; b) **2**•6PF$_6$. Calculated for $C_{72}H_{79}F_{24}N_9O_4P_4$: 856.7405 $[M - 2PF_6]^{2+}$.

4. ^{1}H NMR Spectra of 1•6PF$_6$ and 2•6PF$_6$

The ^{1}H NMR spectra of **1**•6PF$_6$ and **2**•6PF$_6$ with the peak assignments are shown in Figure S3 and S4.

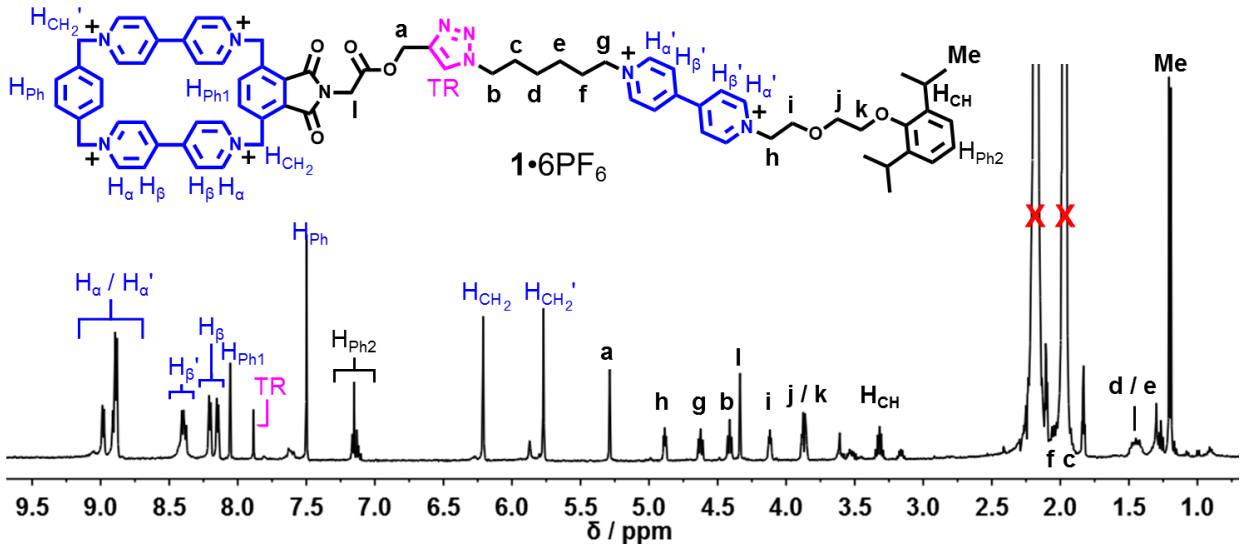

Figure S3. ^{1}H NMR (500 MHz, CD_3CN, 298 K) Spectrum of **1**•6PF$_6$.

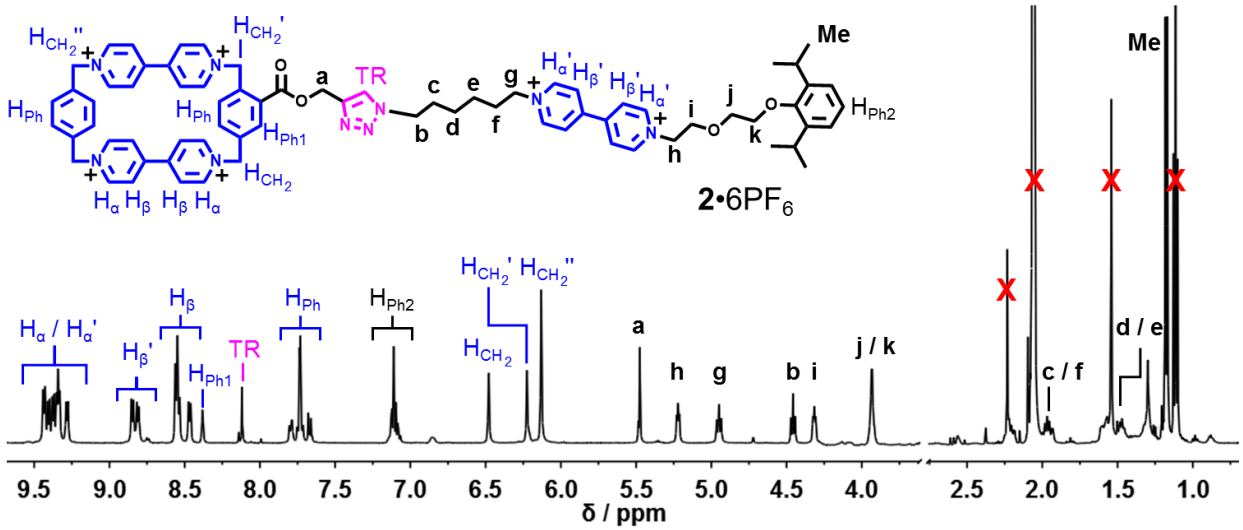

Figure S4. ^{1}H NMR (500 MHz, CD_3COCD_3, 298 K) Spectrum of **2**•6PF$_6$.

5. UV/Vis/NIR Spectroscopic Investigation

In order to verify the formation of the trisradical complex between the half-dumbbell component $\mathbf{5}^{\bullet+}$ and the ring components under reducing conditions, UV/Vis/NIR experiments were carried out (Figure S5) on the solution of (i) individual component and (ii) the equimolar mixture in each case.

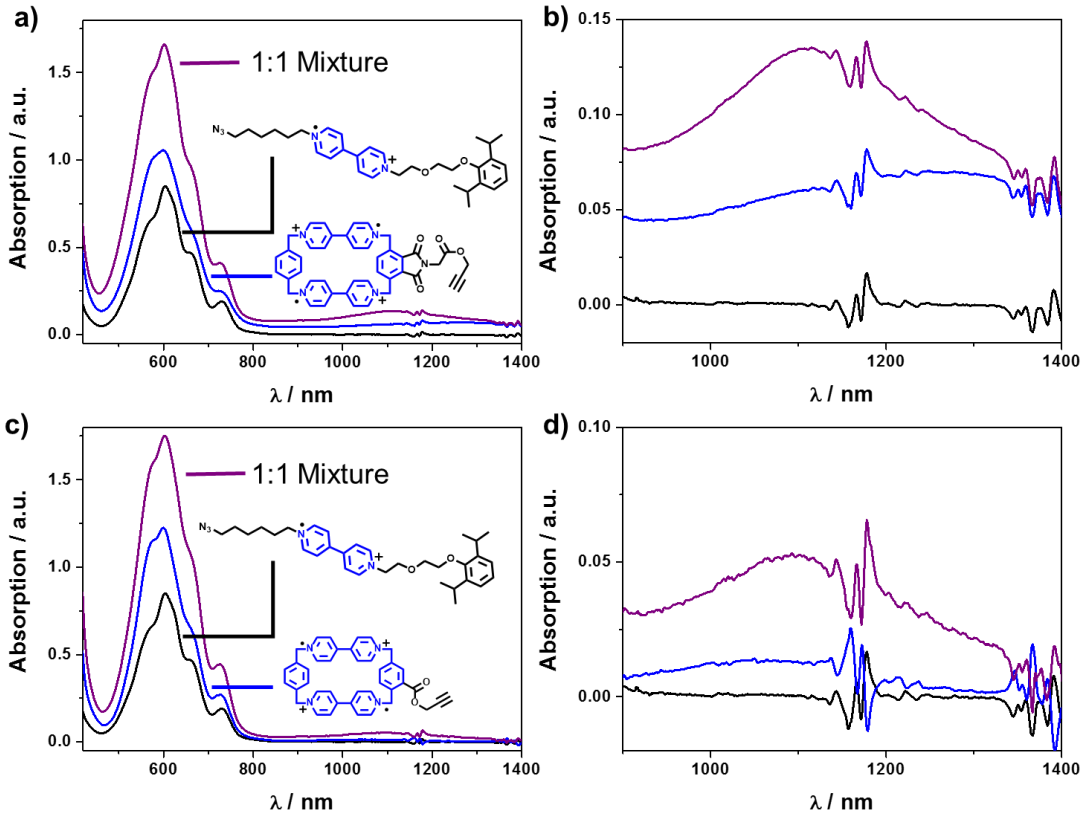

Figure S5. a) UV/Vis/NIR spectra of $\mathbf{5}^{\bullet+}$ (black), $\mathbf{3}^{2(\bullet+)}$ (blue) and an equimolar mixture of $\mathbf{5}^{\bullet+}$ and $\mathbf{3}^{2(\bullet+)}$ (purple) in MeCN. c) UV/Vis/NIR spectra of $\mathbf{5}^{\bullet+}$ (black), $\mathbf{4}^{2(\bullet+)}$ (blue) and an equimolar mixture of $\mathbf{5}^{\bullet+}$ and $\mathbf{4}^{2(\bullet+)}$ (purple) in MeCN. The concentration of each species is 50 µM. b, d) Enlargement of the spectra a) and c) from 900 to 1400nm.

It turns out that at a concentration of 50 µM, when only the half-dumbbell component ($\mathbf{5}^{\bullet+}$, Figure S5, black traces) or the ring components ($\mathbf{3}^{2(\bullet+)}$, Figure S5a-b, blue traces and $\mathbf{4}^{2(\bullet+)}$, Figure S5c-d, blue traces) is present in solution, absorption bands centered at 600 nm, which are characterized as the absorption of $BIPY^{\bullet+}$ radical cations, emerge. In addition, no absorption band above 1000 nm is seen (Figure S5b, d), an observation which indicates the lack of radical-pairing interactions

in the solution. By contrast, upon mixing the half-dumbbell and the ring components together, regardless which ring component, an absorption band centered around 1100 nm (Figure S5a-d, purple traces) emerges, indicating that both ring components are capable of forming inclusion complexes with the half-dumbbell component as a result of radical-pairing interactions.

6. UV/Vis/NIR Absorption Spectrophotometric Titration of $5^{\bullet+}$ by $3^{2(\bullet+)}$ and $4^{2(\bullet+)}$

Figure S6a and S6b show a spectrophotometric titration of $\mathbf{3}^{2(\bullet+)}$ into a MeCN solution of $\mathbf{5}^{\bullet+}$. Upon adding $\mathbf{3}^{2(\bullet+)}$, the absorption of the resulting mixture grows its intensity at 1093 nm, and gradually reaches a saturation point after the addition of 8 equiv of $\mathbf{3}^{2(\bullet+)}$. This data was used for calculating a binding constant (K_a) of 3.0 ±0.9 ×10^4 M^{-1} between $\mathbf{5}^{\bullet+}$ and $\mathbf{3}^{2(\bullet+)}$ based on the 1:1 binding model.

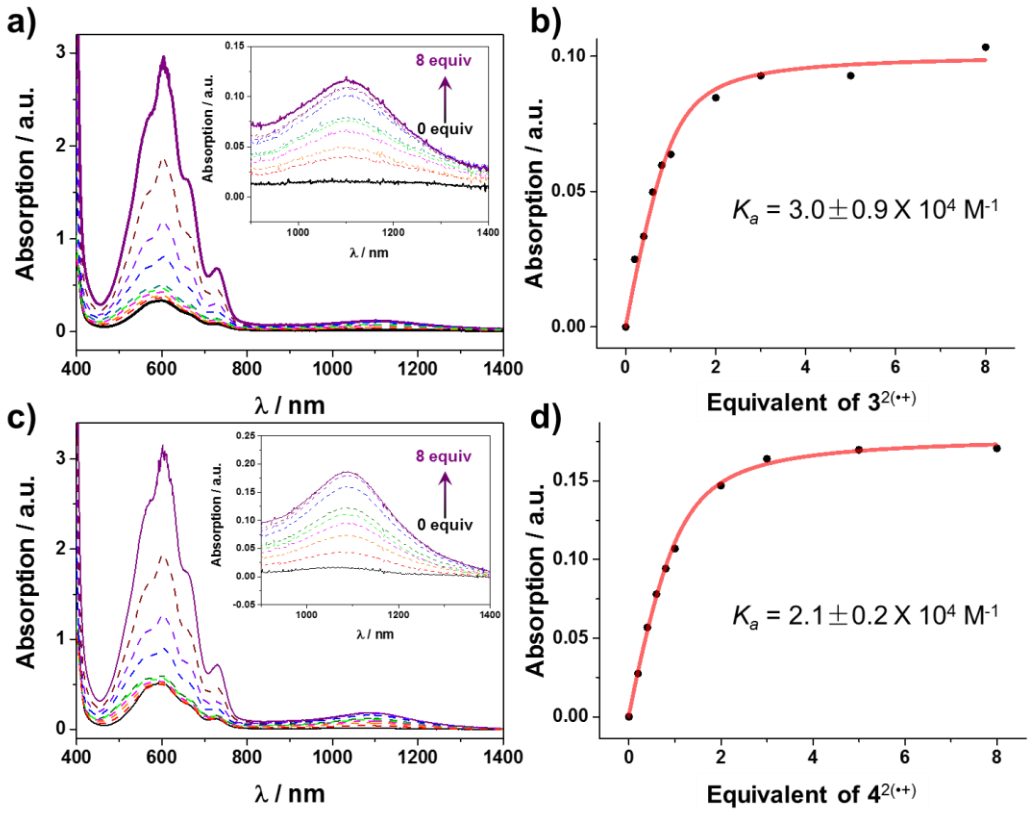

Figure S6. UV/Vis/NIR Absorption spectrophotometric titration experiment of $\mathbf{5}^{\bullet+}$ by a) $\mathbf{3}^{2(\bullet+)}$ and b) $\mathbf{4}^{2(\bullet+)}$. Solvent: MeCN; black: [$\mathbf{5}^{(\bullet+)}$] = 50 μM; purple: c ($\mathbf{3}^{2(\bullet+)}$ or $\mathbf{4}^{2(\bullet+)}$) / c ($\mathbf{5}^{\bullet+}$) = 8. c) The simulated curve for the determination of the binding constant between $\mathbf{5}^{\bullet+}$ and $\mathbf{3}^{2(\bullet+)}$. d) The simulated curve for the determination of the binding constant between $\mathbf{5}^{\bullet+}$ and $\mathbf{4}^{2(\bullet+)}$.

Similarly, the binding constant between $\mathbf{5}^{\bullet+}$ and $\mathbf{4}^{2(\bullet+)}$ was also determined (Figure S6c, d). It turns out that compared with $\mathbf{3}^{2(\bullet+)}$, $\mathbf{4}^{2(\bullet+)}$ binds with $\mathbf{5}^{\bullet+}$ with comparably strong strength (K_a = 2.1 ± 0.2 ×10^4 M^{-1}) in MeCN solution. This observation indicates that the structural differences between these two rings have no significant effect on the strength of radical-pairing interactions, hence demonstrating that the trisradical complexation in $\mathbf{1}^{3(\bullet+)}$ is prevented—by the bulkier linker when compared with $\mathbf{2}^{3(\bullet+)}$—between the half-dumbbell and the ring components.

7. Electrochemical Studies

Evidence for the trisradical complexation between $\mathbf{5}^{\bullet+}$ and $\mathbf{3}^{2(\bullet+)}$ was also obtained by CV experiment. $\mathbf{5}^{2+}$ undergoes (Figure S7, blue trace) two consecutive reversible single-electron reduction process at –441 and –866 mV, corresponding to the redox couples $\mathbf{5}^{2+}/\mathbf{5}^{\bullet+}$ and $\mathbf{5}^{\bullet+}/\mathbf{5}^{0}$ respectively. $\mathbf{3}^{4+}$ also shows (Figure S7, red trace) two reversible two-electron processes, which are slightly anodically shifted[5] compared with those of CBPQT^{4+}, possibly because the electron-withdrawing effect of the imide group in $\mathbf{3}^{4+}$ leads to it having a higher tendency to be reduced.

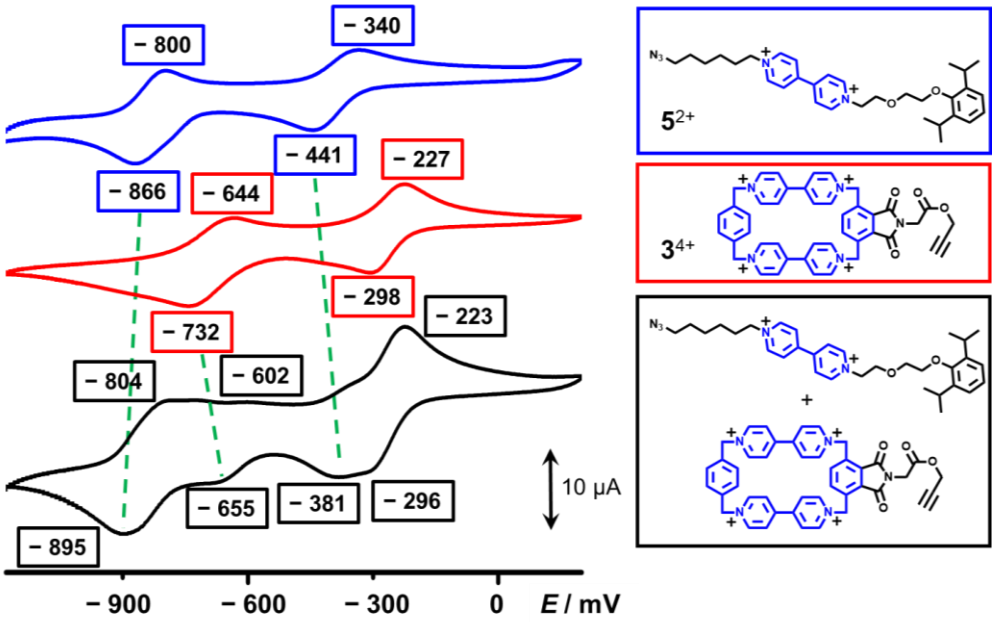

Figure S7. Cyclic voltammograms of compound $\mathbf{5}^{2+}$ (blue), $\mathbf{3}^{4+}$ (red) and an equimolar mixture of $\mathbf{5}^{2+}$ and $\mathbf{3}^{4+}$ (black). The green dash lines denote the potential shifts between the individual species and the equimolar mixture. A glassy carbon working electrode, a platinum counter electrode, and a Ag/AgCl reference electrode were used in the characterization of 0.25 mM MeCN solutions of each species at 298 K with 0.1 M $TBAPF_6$ serving as the electrolyte. A scan rate of 200 mV s^{-1} was used in all the analyses.

On combining an equimolar amount of $\mathbf{5}^{2+}$ and $\mathbf{3}^{4+}$, the CV profile (Figure S7, black trace) of this mixture is not simply the superposition of the two CV profiles recorded for the individual species. Indeed, the mixture first of all undergoes a two-electron reduction process to generate $\mathbf{3}^{2(\bullet+)}$ at – 296 mV, then another electron goes into $\mathbf{5}^{2+}$ at –381 mV, a potential with a +60 mV shift compared with the free $\mathbf{5}^{2+}$, suggesting the radical species are stabilized through the formation of the trisradical inclusion complex $\mathbf{5}^{\bullet+}\subset\mathbf{3}^{2(\bullet+)}$. Next, the trisradical complex $\mathbf{5}^{\bullet+}\subset\mathbf{3}^{2(\bullet+)}$ undergoes further reduction in a stepwise manner to generate its neutral state. It is also noteworthy that the potential to reduce the equimolar mixture from the radical cationic state to the neutral state, i.e., – 895 mV, is lower than that of each free species (– 866 mV for $\mathbf{5}^{2+}$ and – 732 mV for $\mathbf{3}^{4+}$), demonstrating its higher resistance to further reduction, which can also be ascribed to the stabilizing influence of the $\mathbf{5}^{\bullet+}\subset\mathbf{3}^{2(\bullet+)}$ complex.

8. Differential Pulse Voltammetric Characterization of 1•6PF$_6$ and 2•8PF$_6$

In order to gain a better understanding of the electron transfer processes taking place during the formation of the radical states of these two actuators, as well as elucidating how the steric factor associated with the ring components affect the electron transfer mechanism, differential pulse voltammetric (DPV) experiments were performed on **1**•6PF$_6$ and **2**•8PF$_6$. The DPV profile of **1**•6PF$_6$ shows (Figure S8a) five peaks during the reduction process. The 2:1:1:1:1 ratio obtained on integration of each peak suggests that, upon reduction, the hexacation $\mathbf{1}^{6+}$ first of all receives two electrons to generate the diradical $\mathbf{1}^{2(\bullet+)2+}$, which is further reduced in a stepwise manner through four single-electron-oxidation processes, giving rise to the formation of the fully reduced state $\mathbf{1}^{(0)}$. The DPV profile of **2**•8PF$_6$ demonstrates (Figure S8b-c) a similar electron transfer mechanism. Comparison of the relative integrations associated with each peak reveals a 2:1:1:2 ratio in relation to the numbers of electrons. This result indicates that, upon reduction, $\mathbf{2}^{6+}$ was first of all converted to the diradical state $\mathbf{2}^{2(\bullet+)2+}$ by a two-electron process, followed by a single-electron process to give the the trisradical state $\mathbf{1}^{3(\bullet+)}$. The trisradical species $\mathbf{1}^{3(\bullet+)}$ then undergoes a single and a double-electron reduction process to generate the fully reduced state $\mathbf{1}^{(0)}$.

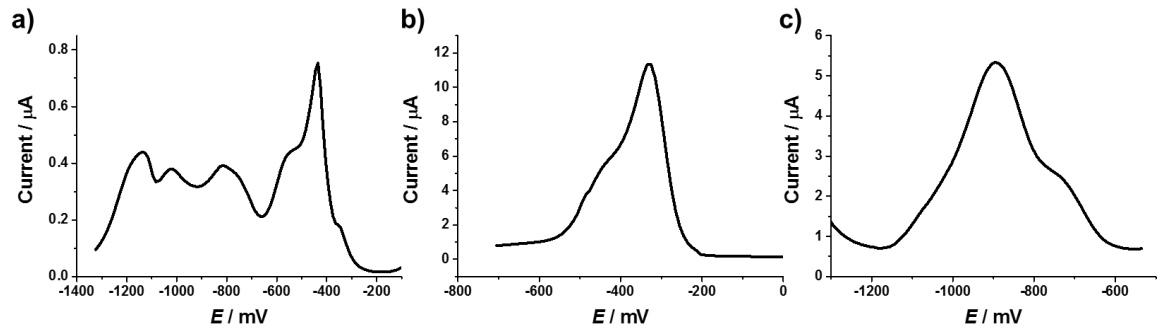

Figure S8. a) DPV Profile of **1**•6PF_6. The ratio of the area under each peak (from right to left) is 2:1:1:1:1. b-c) DPV Profiles of **2**•6PF_6. The ratio of the area under each peak (from right to left) is 2:1 in b) and 1:2 in c).

9. ^{1}H NMR Spectroscopic Investigation of 1•PF_6 and 2•PF_6

In order to confirm the redox-controlled actuations of $\mathbf{1}^{6+}$ and $\mathbf{2}^{6+}$ are reversible by altering the external potential, their ^{1}H NMR spectra were recorded (i) before the reduction by Zn dust, and (ii) after the re-oxidation of the radical cationic states by air.

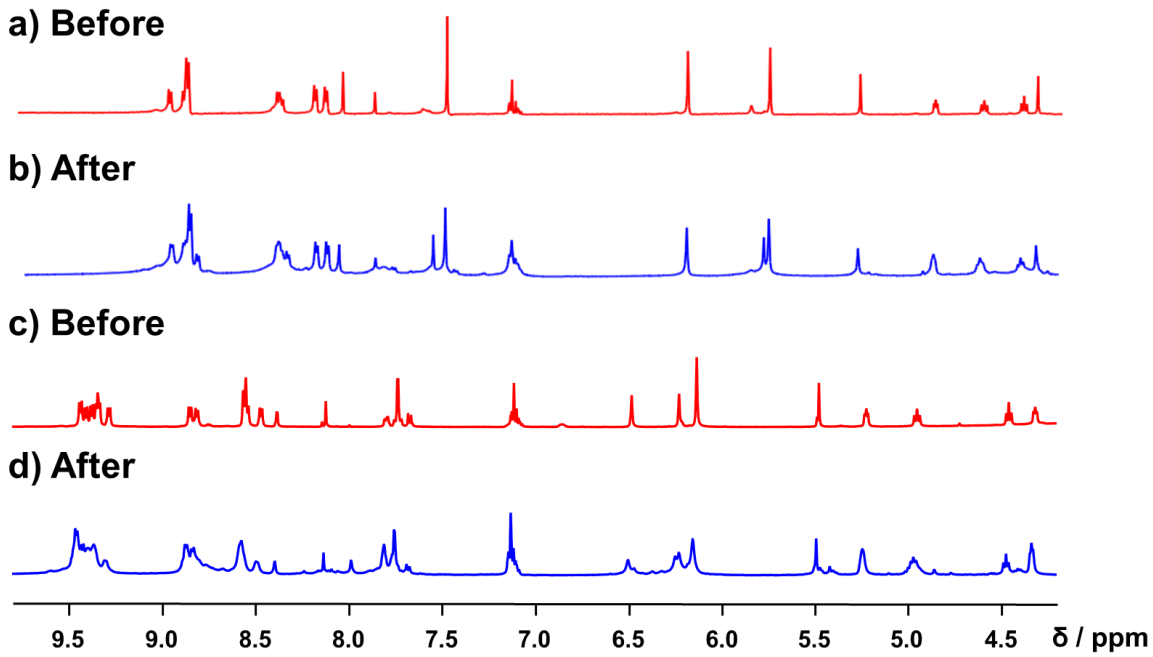

Figure S9. ^{1}H NMR spectra of $\mathbf{1}^{6+}$ obtained in CD_3CN at 298 K a) before the reduction, and b) after the re-oxidation of $\mathbf{1}^{3(\bullet+)}$ by air.^{1}H NMR spectra of $\mathbf{2}^{6+}$ obtained in CD_3COCD_3 at 298 K c) before the reduction, and d) after the re-oxidation of $\mathbf{2}^{3(\bullet+)}$ by air.

Figure S9 shows that in both cases, the ^{1}H NMR spectra give almost identical signals before and after the redox-controlled actuation process, demonstrating that these actuation processes are reversible.

10. Investigation of the Stabilities of $\mathbf{1}^{3(\bullet+)}$ and $\mathbf{2}^{3(\bullet+)}$ in the Air

In order to investigate how the different self-complexing properties of $\mathbf{1}^{3(\bullet+)}$ and $\mathbf{2}^{3(\bullet+)}$ can affect the stabilities of the $BIPY^{\bullet+}$ radical species, we prepared two CD_3CN solutions (1mL) of **1**•$6PF_6$ (2.1 mg) (Figure S10a–i, left vial) and **2**•$6PF_6$ (2.0 mg) (Figure S10a–i, right vial) respectively under an atmosphere of Ar.

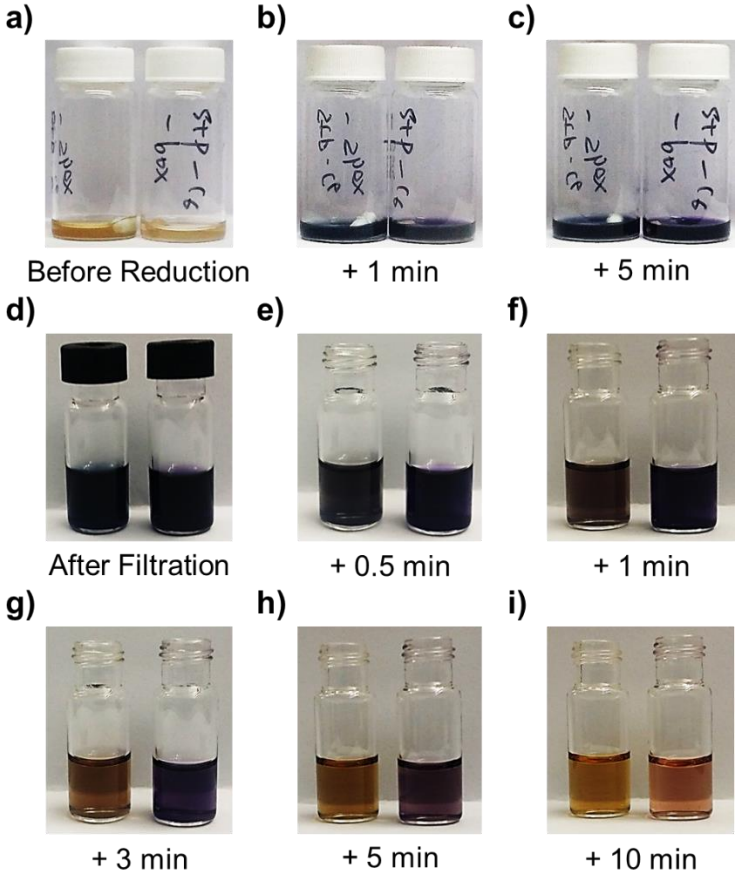

Figure S10. Photographs of the CD_3CN solutions (1 mL) of **1**•$6PF_6$ (left vial) and **2**•$6PF_6$ (right vial) that taken a) before the addition of the Zn dust, b) 1, c) 5 min after the addition of an excess of Zn dust, d) after the filtration of the Zn dust, e) 0.5, f) 1, g) 3, h) 5 and i) 10 min after exposing the CD_3CN solutions to the oxygen in the air.

Both solutions were treated with an excess of Zn dust (Figure S10a–c), during which time their colors were monitored (Figure S10a–c) visually at 1 and 5 min. The Zn dust in both solutions was then filtered off, and the solutions were transferred (Figure S10d) to another two vials and exposed to the air. The colors of both solutions were monitored (Figure S10a–c) visually over time. The pictures show (Figure S10b-c) that both solutions with Zn dust turned dark purple after 1 min, indicating both **1**•6PF_6 and **2**•6PF_6 can be converted rapidly to their radical cationic states upon reduction. By comparison, the two molecular actuators show (Figure S10e-i) different behavior upon re-oxidation. While the re-oxidation of the solution of $\mathbf{1}^{3(\bullet+)}$—indicated by the fading of the purple color—took place (Figure S10e) right after (< 0.5 min) its exposure to the oxygen and was (Figure S10g) nearly completed after 3 min, the solution of $\mathbf{2}^{3(\bullet+)}$ showed a much higher resistance to oxidation by oxygen, since the purple color of the solution can still be observed (Figure S10h-i) after 5 min of exposure. This observation is in a good agreement with the results of the CV experiments, which demonstrates that the self-interlaced structure of $\mathbf{2}^{3(\bullet+)}$ results in the higher stability of the radical species.

11. X-Ray Crystallography

Crystallization Procedure: A 1 mM MeCN solution of **3**•4PF_6 was filtered through a Pall syringe filter (pore size 0.45 μm) into VWR culture tubes (6 × 50 mm). The tubes were allowed to stand at room temperature in a closed scintillation vial containing *i*Pr_2O (3 mL). After one week, colorless crystals of **3**•4PF_6 appeared in the tubes from which a rod-like crystal was picked out and mounted using oil (Infineum V8512) on a glass fiber and transferred to the cold gas stream, cooled by liquid N_2 on a Bruker APEX-II CCD with graphite monochromated Mo-Kα radiation. The structure was solved by direct methods and refined subsequently using the OLEX2 software.[6]

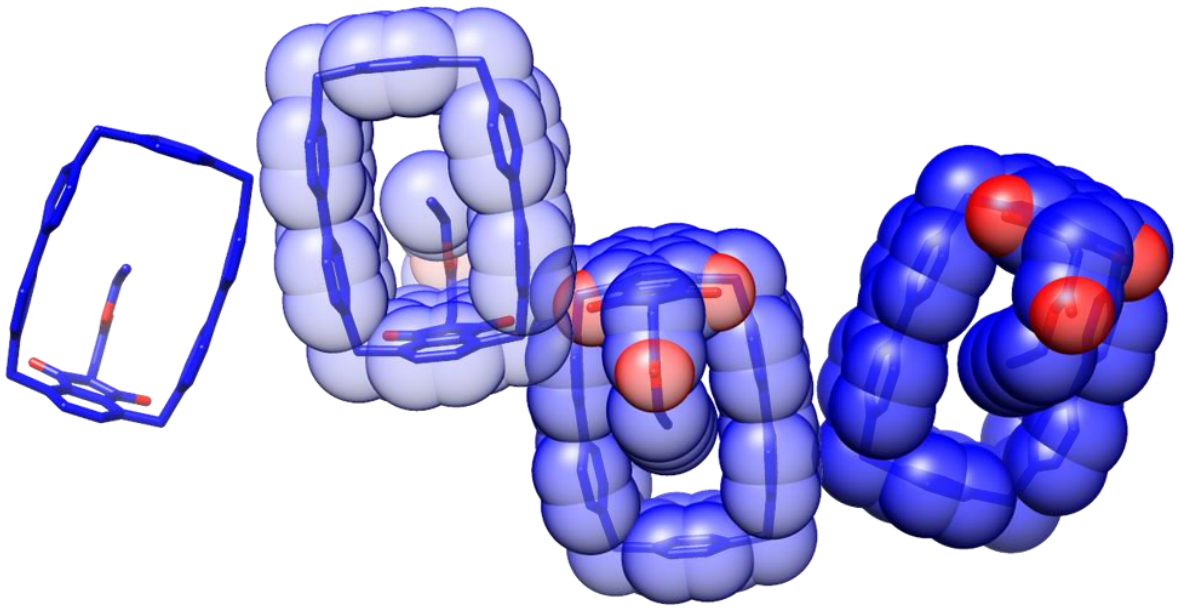

Figure S11. Side-on views of the solid-state superstructures of 3^{4+}. The PF_6^- counterions are omitted for the sake of clarity.

The packing of $\mathbf{3}^{4+}$ shows (Figure S11) that the orientation of the loop is not well aligned because of the bulky imide group and the strong Coulumbic repulsion between the $BIPY^{2+}$ units. It is also noteworthy that, despite the alkyne proton of $\mathbf{3}^{4+}$ being directed inwards (Figure 4a) towards the centre of the loop, no $\mathbf{1}^{6+}$ with a self-entangling lasso-like conformation, in which the half-dumbbell approaches from the other side of the loop to form the triazole ring, was observed in the reaction mixture during its synthesis—a phenomenon which can be ascribed to the dynamic motion of $\mathbf{3}^{4+}$ in solution and the extremely low probability of statistical threading of the $CBPQT^{4+}$ loop by the azide.

Crystal Data for **3**•4PF_6: $C_{43}H_{35}F_{24}N_5O_4P_4$, M =1265.13, crystal size 0.312 × 0.247 × 0.044 mm^3, monoclinic, space group $P2_1/n$ (no. 14), a = 10.6431(11), b = 41.576(4), c = 13.8546(15) Å, α = 90, β = 110.763(5), γ = 90 °, V = 5732.4(10) $Å^3$, T = 100.02 K, Z = 4, ρ_{calc}= 1.607 g/mm^3. Of a total of 101667 reflections that were collected ($1.96 \leq 2\Theta \leq 60.004$), 16706 were unique ($R_{int}$ = 0.0614, R_{sigma} = 0.0539). Final R_1 ($F^2 > 2\sigma F^2$) = 0.0945, wR_2 = 0.3014. CCDC number: 1517068. Data

were collected at 100 K using a Bruker d8-APEX II CCD diffractometer. Intensity data were collected using ω and φ scans spanning at least a hemisphere of reciprocal space for all structures (data were integrated using SAINT). Absorption effects were corrected on the basis of multiple S13 equivalent reflections (SADABS). The structure was solved by direct methods (SHELXS) and refined by full-matrix least-squares against F2 (SHELXL).

References

1. A. B. Braunschweig, W. R. Dichtel, O. Š. Miljanić, M. A. Olson, J. M. Spruell, S. I. Khan, J. R. Heath and J. F. Stoddart, *Chem. –Asian. J.*, 2007, **2**, 634.
2. H. Li, A. C. Fahrenbach, A. Coskun, Z. Zhu, G. Barin, Y.-L. Zhao, Y. Y. Botros, J.-P. Sauvage and J. F. Stoddart, *Angew. Chem. Int. Ed.*, 2011, **50**, 6782.
3. Z. Zhu, H. Li, Z. Liu, J. Lei, H. Zhang, Y. Y. Botros, C. L. Stern, A. A. Sarjeant, J. F. Stoddart and H. M. Colquhoun, *Angew. Chem. Int. Ed.*, 2012, **51**, 7231.
4. M. M. Boyle, J. J. Gassensmith, A. C. Whalley, R. S. Forgan, R. A. Smaldone, K. J. Hartlieb, A. K. Blackburn, J.-P. Sauvage and J. F. Stoddart, *Chem.–Eur. J.*, 2012, **18**, 10312.
5. A. Trabolsi, N. Khashab, A. C. Fahrenbach, D. C. Friedman, M. T. Colvin, K. K. Cot ́ı D. Ben ́ez, E. Tkatchouk, J.-C. Olsen, M. E. Belowich, R. Carmielli, H. A. Khatib, W. A. Goddard, III., M. R. Wasielewski and J. F. Stoddart, *Nat. Chem.*, 2010, **2**, 42.
6. Dolomanov, O. V., Bourhis, L. J., Gildea, R. J, Howard, J. A. K. and Puschmann, H. *J. Appl. Cryst*. **2009**, *42*, 339.